Comparative Analysis of Fatigue Life Predictions in Lateral Notched Round Bars under Multiaxial Loading

R. Branco, J.D. Costa, F.V. Antunes, P. Bento

The main objective of this study is to predict the multiaxial fatigue life for lateral notched round bars made of DIN 34CrNiMo6 high strength steel. In-phase bending-torsion tests for different stress amplitudes and different ratios of the normal stress to the shear stress were performed. Single torsion and single bending tests were also conducted for different stress amplitudes. In addition, the beach marking technique was used to mark crack fronts on fracture surfaces for the different loading paths studied. Experimental fatigue life was compared with predictions obtained by the Coffin-Manson model. The stress-strain state at the notch root was evaluated using the Theory of Critical Distances (TCD) and the Equivalent Strain Energy Density (ESED). Finally, a comparative analysis of the fatigue life predictions obtained by the two above-mentioned approaches was carried out. The former gave good results for higher lives but was too conservative for lower lives. The latter led to good correlations in the range studied here.

1 Introduction

DIN 34CrNiMo6 high strength steel is a very versatile engineering material. It combines high ductility, deep hardenability, toughness and strength. Due to above-mentioned properties, it is ideal for critical components working under severe service conditions, for instance shafts, axles, crankshafts, connecting rods, pinions, torsion bars, bolts, aircraft components, high pressure vessels for nuclear plants, among others. In general, such components have geometric discontinues, generally termed notches, and are often subjected to relatively complex loading. These characteristics make them susceptible to fatigue failure. For the material studied in this research, there are many cases of fatigue failure reported in the literature. In the last few years, some critical examples are drive shafts (Savković, 2012), connecting rods (Griza, 2009), diesel generator crankshafts (Espadafor, 2009), train axles (Yu, 2009), bolts and pins (Yu, 2008), fuselage connectors (Witek, 2006) and aircraft main landing gears (Eliaz, 2005).

In notched components, the highest stresses and strains are found close to the notch root. Due to stress and strain concentration phenomena, nominal elastic stresses can result in elastic-plastic stress-strain fields around the notch. The fatigue damage accumulation caused by cyclic loading at the notch root is likely to lead to crack initiation and crack propagation which can culminate in fatigue failure. Unexpected in-service fatigue failure can cause not only a large loss of money but also loss of lives. Therefore, a crucial task in the design of notched components is an effective evaluation of the fatigue life. Nevertheless, fatigue phenomenon is a complex problem since it depends on many variables, namely the notch geometry, the loading type, the loading magnitude, and the cyclic material behaviour, among others.

The fatigue behaviour of engineering components subjected to multiaxial loading is not easily described due to the complex cyclic stress-strain response of the materials. Although there are a significant number of multiaxial fatigue models in the scientific literature, there is no consensus on a universally accepted model (Garud, 1981; You, 1996). Existing models can be classified into stress-based, strain-based and energetic-based approaches. An extensive overview on multiaxial fatigue models can be found elsewhere (Socie, 2000).

However, the aforementioned approaches neglect the effect of notch geometry on crack behaviour. Although the fatigue behaviour of notched components subjected to multiaxial loading has been handled by many authors, cases involving combined bending-torsion rarely have been addressed in the literature. Gough (1949) discussed the influence of different bending and torsion loadings on fatigue life for components with different notch configurations, such as oil holes, sharp transition fillets and splines, among others. Fash *et al*. (1985) evaluated the fatigue life for solid notched shafts subjected to bending-torsion using five different strain-based approaches

and found errors up to 10 times in terms of fatigue life. Tripton *et al.* (1985) studied the fatigue life prediction for solid round specimens with a shoulder fillets under different in-phase and out-of-phase combined bending-torsion loadings using different stress-based and strain-based approaches. Park *et al.* (2000) applied stress-based, energy-based and critical plane based approaches to predict multiaxial fatigue life in solid round bars having circumferential semi-circular grooves subjected to combined bending-torsion. Costa *et al.* (2005) analysed the fatigue behaviour of tubular welded specimens under in-phase combined bending-torsion loading using both the stress-strain field intensity and the equivalent strain energy density approaches. The former gave better results than the latter when compared with the experimental fatigue lives. Abreu *et al.* (2009) focused on the fatigue behaviour of welded and notched tubular specimens made of aluminium alloy experiencing different in-phase bending-torsion paths. The fatigue life predictions were carried out from the stress-strain field intensity approach and a novel energy-based approach. In both cases, reasonable predictions in terms of fatigue life were found. Firat (2012) predicted the fatigue life for a solid round bar with a circumferential semi-circular notch under combined bending-torsion using two critical plane criteria. For both in-phase and out-of-phase tests, predictions were in line with the experimental fatigue lives.

The studies referred to above have been mainly focused on round bars with circumferential notches or transverse circular holes. However, mechanical components also contain solid circular cross-sections with lateral notches. In this sense, the study of these geometries in terms of multiaxial fatigue is a matter of great importance. The present paper addresses the fatigue life prediction for lateral notched round bars made of DIN 34CrNiMo6 high strength steel subjected to bending-torsion loading. Three different ratios of the bending moment to the torsion moment were studied for different stress amplitudes. Single torsion and single bending tests were also conducted. In order to better understand the effect of the loading path on the crack front shape, the beach marking technique was used to mark crack fronts on fracture surfaces. Experimental fatigue life was compared with predictions obtained with the well-known Coffin-Manson model. The stress-strain state at the notch root was evaluated using the Theory of Critical Distances (TCD) and the Equivalent Strain Energy Density (ESED). Finally, a comparative analysis of the fatigue life predictions obtained by the two above-mentioned approaches was carried out.

2   Experimental Procedure

The material investigated in this research was a DIN 34CrNiMo6 high strength steel. The nominal chemical composition and the mechanical properties are listed in Table 1 and Table 2, respectively. In general, it is employed in the manufacture of critical components that operate under severe service conditions, such as axles, shafts, crankshafts, connecting rods, valves, propeller hubs, gears, couplings, torsion bars, landing gears, heavy duty parts of rock drills, among others.

The specimens were machined in a computer numeric control turning centre from 20mm-diameter round bars. Before testing, the notch surfaces were carefully polished, firstly, with a high-speed mechanical polishing using successively 600, 1200 and 2500 grit silicon carbide papers, and then using 6 μm diamond paste.

The specimen geometries used are schematised in Figure 1(a) and Figure 1(b). The geometry of Figure 1(a) consists of a 16mm-diameter round bar with a lateral notch. The notch has a U-shape with diameter and depth of 3 mm and is placed asymmetrically with respect to the longitudinal centre of the specimen only to facilitate mounting and observation during the test. The geometry of Figure 1(b) has a smaller diameter. The notch is

Table 1. Nominal chemical composition of DIN 34CrNiMo6 in weight percentage (Branco, 2012)

C	Si	Mn	Cr	Mo	Ni
0.34	≤ 0.40	0.65	1.50	0.22	1.50

Table 2. Monotonic mechanical properties of DIN 34CrNiMo6 high strength steel (Branco, 2012)

Yield strength, σ_{YS} [MPa]	967	Fatigue strength coefficient, σ_f' [MPa]	1183.7
Ultimate tensile strength, σ_{UTS} [MPa]	1035	Fatigue strength exponent, b	-0.0545
Elongation, ε_R (%)	18	Fatigue ductility coefficient, σ_f'	0.4697
Reduction of area (%)	58	Fatigue ductility exponent, c	-0.6059
Young's modulus, E [GPa]	209.8	Cyclic hardening coefficient, k' [MPa]	1361.6
Poisson's ratio, ν	0.296	Cyclic hardening exponent, n'	0.1041

similar, having the same diameter, the same depth and the same location. The change in geometry aimed at reducing the contact friction force between the specimen ends and the machine grips. The former geometry was used in single bending and in-phase combined bending-torsion tests, whilst the latter was used in single torsion.

Five different proportional loadings were studied, namely single bending, single torsion and three in-phase combined bending-torsion paths. Regarding the last type, the ratios of the bending moment (B) to the torsion moment (T) adopted were, i.e. B=2T, B=T and B=2T/3. These relations, in terms of normal stress to shear stress ratio, correspond to $\sigma=4\tau$, $\sigma=2\tau$ and $\sigma=4\tau/3$, respectively. All loading paths were examined for three stress levels. Tests were conducted in load control, under constant amplitude load, with values of stress ratio (R) close to zero in order to avoid fluctuations of the gripping system during the absence of loading. Sinusoidal load waves and frequencies of about 3-6 Hz were used. All these tests were performed on a conventional servo-hydraulic machine (Figure 2(a)) coupled to a special gripping system that could be assembled in three different ways, as displayed in Figures 2(b)-2(d). In the bending-torsion tests, the B/T ratio could be changed by moving the screw (Figure 2(d)) in the slot. The B/T ratio was increased by moving the screw to the left and vice versa. Figure 2(d) presents, as an example, the gripping system assembled for the case B=2T.

The detection of crack initiation as well as the crack growth observation were performed in-situ with a digital monitoring system consisting of a high performance 14-bit charge-coupled digital camera (pco.pixelfly usb) and an optical device with variable magnification (Specwell M850-S) coupled to a micrometre driven translation stage supplied by the Parker Hannifin Corporation (Model M4424). In all tests, the notch was placed upside down (Figure 2(a)) and the digital monitoring system was located immediately below. Therefore, the relative position of the notch with respect to the digital monitoring system was always the same, regardless of the loading path. Apart from the software of the digital monitoring system, a manual diaphragm incorporated into the optical device and a manual focus system were also used to optimise image quality. In addition, a fine layer of blue ink mixed with acetone was deposited on the surface of the notch allowing a more uniform reflection of light.

Digital images were recorded in a systematic manner using an exposure time of 1s and were captured every 5×10^3 cycles. After crack detection, usually for surface cracks having a length of 200-300 μm, the interval was reduced to 2×10^3 cycles. In the final stage of testing, images were recorded every 1×10^3 cycles. In longer tests, i.e., for lives greater than about 150×10^3 cycles, images were acquired every 10×10^3 cycles during the crack initiation period and after that the periodic acquisions were reduced successively to 5×10^3, 2×10^3 and 1×10^3 cycles.
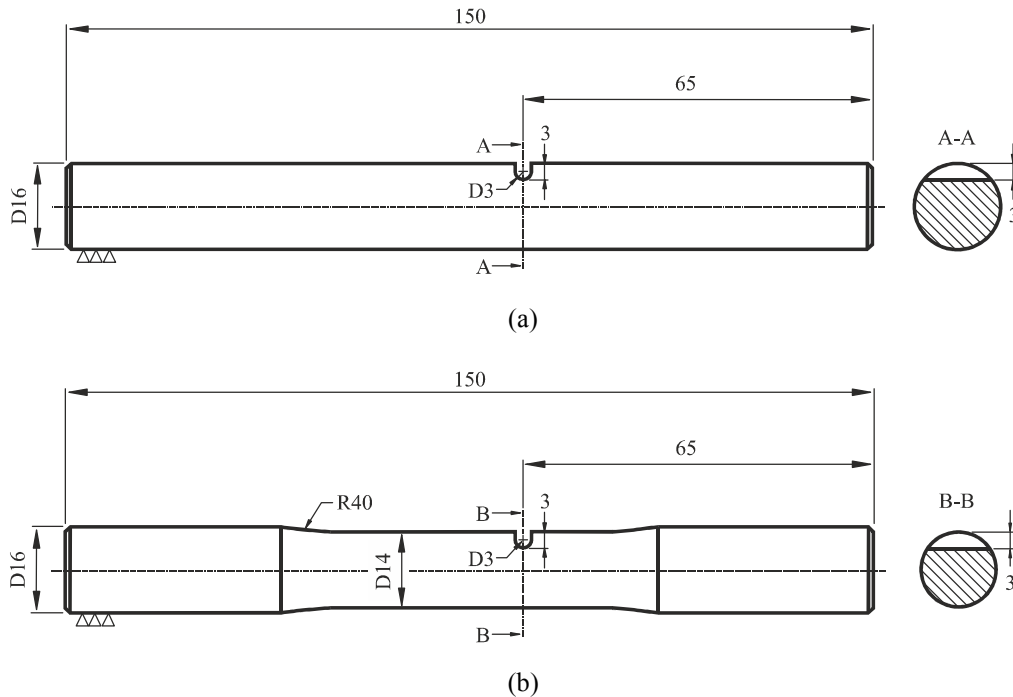

Figure 1. Specimen geometries used in the multiaxial fatigue tests: (a) single bending and bending-torsion; (b) single torsion (dimensions in millimetres)
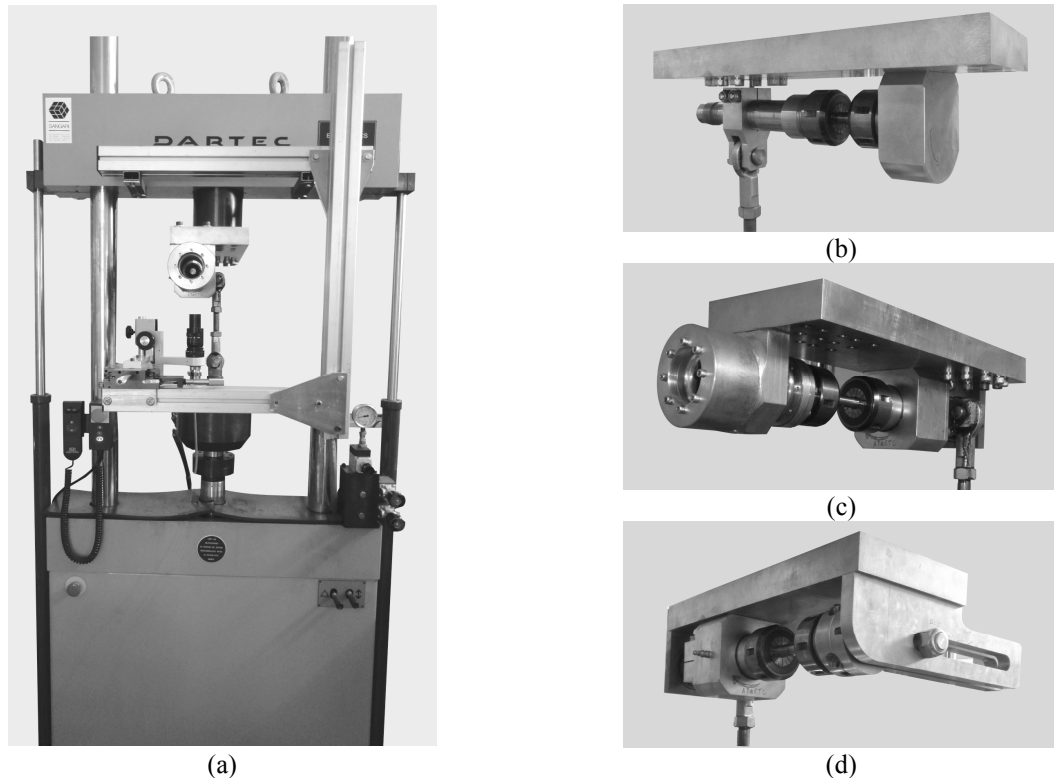
Figure 2. (a) Servo-hydraulic testing machine used in fatigue tests. Details of the gripping system assembled for: (b) single bending; (c) single torsion; (d) in-phase combined bending-torsion (B=2T)

The notch was always observed under the maximum load applied during the test which simplified the in-situ detection of crack initiation. At the time of observation, the cyclic loading was suspended and a static load with a magnitude corresponding to the maximum stress was applied. As a result, the crack remained open as long as necessary which contributed to an easy crack detection and an accurate measurement of the crack length. After crack observation and image recording, the test was resumed. Tests were interrupted before separation of the specimen into two pieces. Final failure was assumed when the piston displacement increased about 25% relatively to the beginning of the test (i.e. undamaged specimen hypothesis). The typical uncracked ligaments observed in these tests varied between 15-25% of the cross-sectional area of the specimens.

In order to better understand the effect of the loading path on the crack shape evolution, additional fatigue tests were carried out to mark crack front profiles on the fracture surfaces. The crack front marking tests were conducted using the beach-marking technique. In particular moments of the test, the applied stress level was changed for several cycles. The change of the loading conditions resulted in particularly well-defined macroscopic progression markings on the fracture surface. The perturbations of the loading were caused by overload blocks applied several times during each test. The number of cycles of the overload blocks was deliberated reduced throughout the test due to the increase of the crack propagation rates. In the first part of the test, when the crack was a surface crack (contained in the notch surface), the overload blocks were applied for surface crack lengths multiples of 2.5 mm with overload ratios of 1.75 (i.e. 75% above the nominal stress range) during at about 100-60 cycles. In the second part of the test, when the crack was a through crack, the crack was measured laterally. The overload blocks were applied when the difference between the current crack length and the crack length of the last overload was roughly equal to 2 mm. In this case, overload ratios of 1.5 were considered and the number of cycles varied between 10 and 3 cycles in order to reduce the risk of fracture in an early stage of the test.

3   Numerical Procedure

The physical model created to simulate the in-phase combined bending-torsion tests is schematised in Figure 3(a). Bending moments (B) were applied by two forces parallel to the axis of the specimen with the same

$F_T = \lambda F_B$

F_B

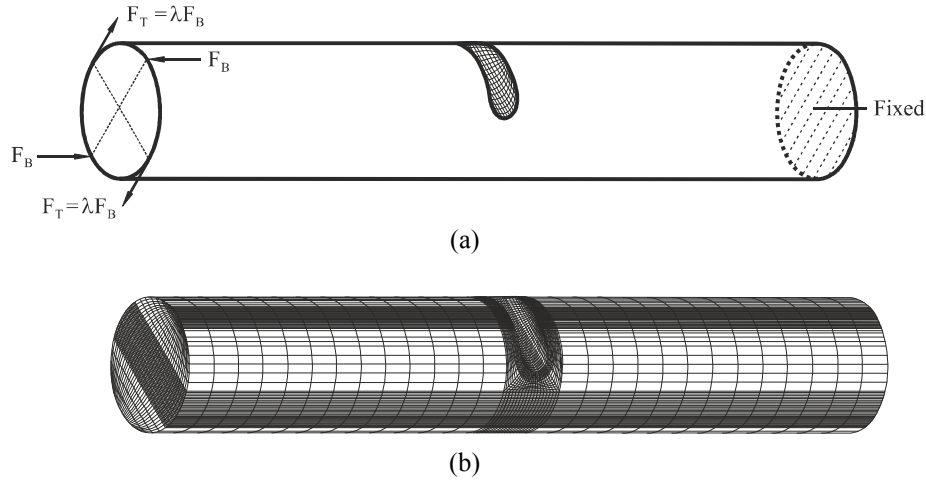F_B

$F_T = \lambda F_B$

Fixed

(a)

(b)

Figure 3. (a) Physical model; (b) finite element model

magnitude and opposite directions. The directions and points of application of this pair of forces were selected to ensure the opening of the notch, i.e. the notch root was subjected to a positive bending stress. Torsion moments (T) were created by a couple of forces with the same magnitude and opposite directions acting on a plane normal to the longitudinal axis of the specimen. The forces were applied at one end of the specimen while the other was fixed, i.e. displacements were restrained. The B/T ratios were defined by changing the value of λ (see Figure 3(a)), which was considered to be equal to 1/2, 1 and 3/2 for the cases B=2T, B=T and B=2T/3, respectively. The physical models for single bending and single torsion only had bending moments or torsion moments, respectively. In the latter case, ends were simplified due to their remote position relatively to the notch root.

Figure 3(b) presents the finite element model created in this study. The mesh was developed using 8-node isoparametric hexahedrical elements. The mesh density resulted from a trade-off between accuracy and efficient computation. As can be seen, it is extremely refined near the notch region in order to obtain accurate results in that zone. In contrast, at remote positions, a coarser mesh was created to reduce the computational effort. The assembled model had 99,823 nodes and 76,608 elements. The material was assumed to be homogeneous and isotropic with a linear regime described by its Poisson's ratio and Young's modulus.

4   Results and Discussion

Figure 4 shows representative fatigue crack paths obtained in the experimental tests for the different loading cases. A significant influence of the loading pattern on the crack trajectory is observed. In the first case (Figure 4(a)), for single bending loading, the crack propagates in a direction approximately normal to the axis of the specimen. In the other cases (Figure 4(b)-(e)), the crack trajectories become more and more curved with the increase of the shear stress to the normal stress ratio. The experimentally detected crack initiation sites, depicted by the white circles, can be seen in Figure 4. Not surprisingly, there is a clear effect of the loading pattern on the initiation process. In the two first cases (Figures 4(a)-(b)), due to the absence or reduced level of shear stresses, the crack initiates in the center of the notch. In the other cases (Figures 4(c)-(e)), the crack initiates close to the curved edge of the notch. The closeness increases with the shear stress to the normal stress ratio.

Both fatigue crack paths and the initiation sites seem to be controlled by the distribution of the principal stresses along the notch surface. The most susceptible regions to crack initiation, obtained using the FEM model described above, are identified by the white squares which correspond to the maximum principal stresses. The dashed white lines, also obtained numerically, represent the most likely crack surface paths. As can be seen in Figure 4, numerical predictions in terms of surface crack paths and crack initiation sites obtained using this approach are very close to those detected experimentally. On the contrary, regardless of the loading scenario, the maximum shear stress is not close to the initiation sites. In the cases B and B=2T (absence or reduced level of shear stress), it is located in the curved edge of the notch while in the other cases, with high levels of shear stress, it occurs in the centre of the notch.

Figures 5(a)-(e) present typical fracture surfaces obtained in the fatigue crack front marking tests for the different loading paths studied in this research. For each case, top and front views are shown. As can be seen, there is a

132

considerable effect of the loading pattern on the fracture surfaces. For single bending (see Figure 5(a)), fracture surfaces are flat and normal to the specimen axis. This is expected since these specimens are under mode I loading. The several steps observed at the surface are reflex of multi-crack initiation which tends to occur in this steel (Tartaglia, 2012). In the other cases (Figures 5(b)-(e)), typical fracture surfaces have increasingly complex shapes due to higher ratios of the shear stress to the normal stress and are the result of out-of-plane propagation.

In relation to the crack front markings, the differences are also clear. In Figure 5(a), the experimental marks are almost semi-elliptical and progressively flatter. This fact can be confirmed in Figure 6, which plots the crack aspect ratio (a/b) against the dimensionless crack length (a/D'). For single bending, as schematised in Figure 6(a), a' and b' represent the semi-axes of an ellipse whose centre is coincident with the origin of the coordinate system and $D' = D-n$ (n is the notch depth). As can be seen, a/b decreases with a/D'. In the other cases (Figures 5(b)-(e)), marks are not symmetric in relation to the half-thickness and are increasingly curved as a consequence of the higher ratios of the shear stress to the normal stress. Figure 6(b) presents the crack aspect ratio (a/b) versus the dimensionless crack length (a/D') for these four loading patterns. The variables a and b, as depicted in Figure 6(a), are the semi-axes of an ellipse whose centre is on the notch root but not necessarily at the half-thickness. Despite the differences in the definition of the crack aspect ratio, it is interesting to note that the a/b values are relatively close for all the loading patterns.
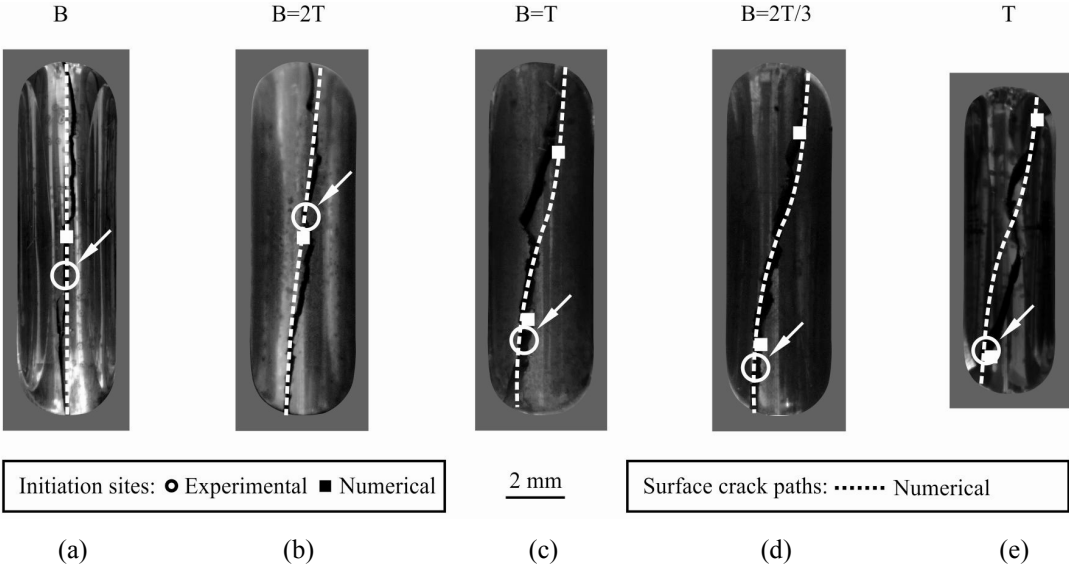

Figure 4. Surface crack paths and initiation sites for different loading patterns (notches observed from top views): (a) B; (b) B=2T; (c) B=T; (d) B=2T3; (e) T
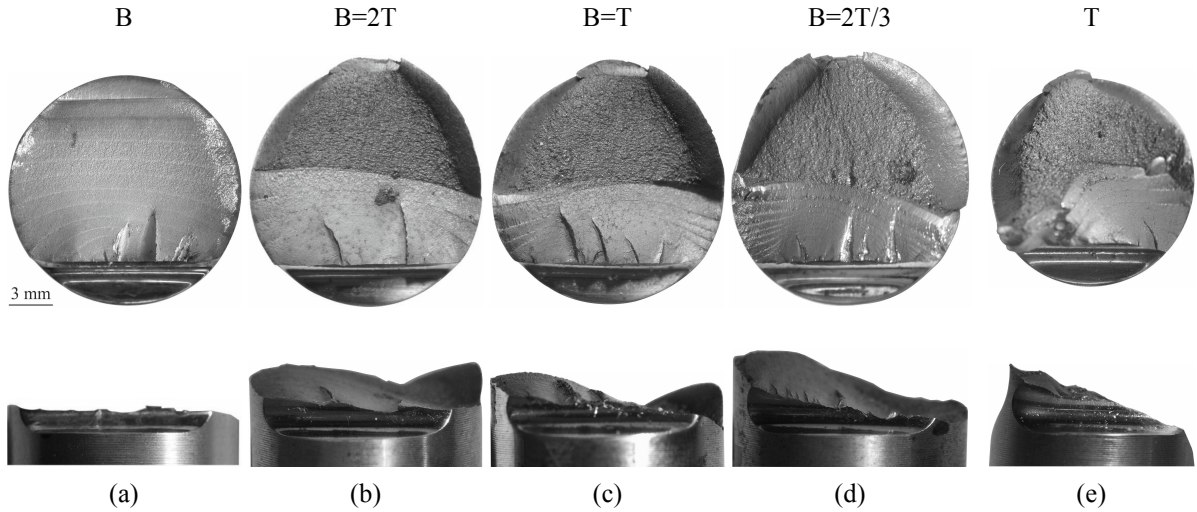

Figure 5. Fracture surfaces of fatigue crack front marking tests for the different loading patterns: a) B; b) B=2T; c) B=T; d) B=2T/3; e) T
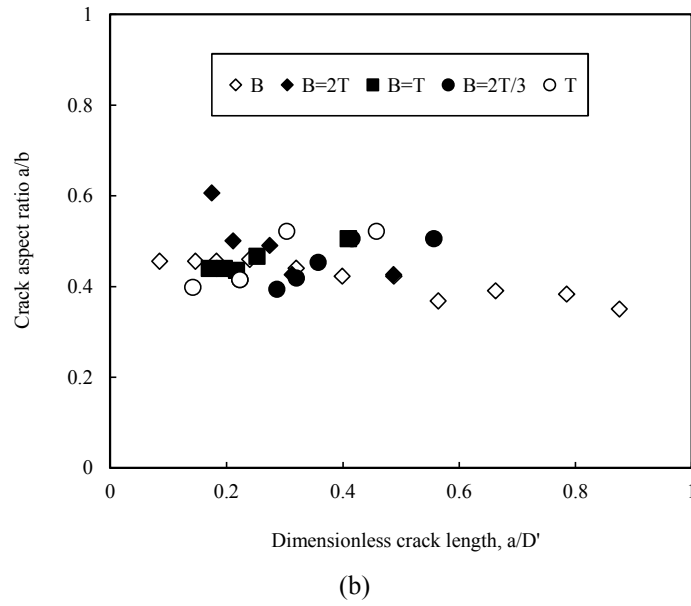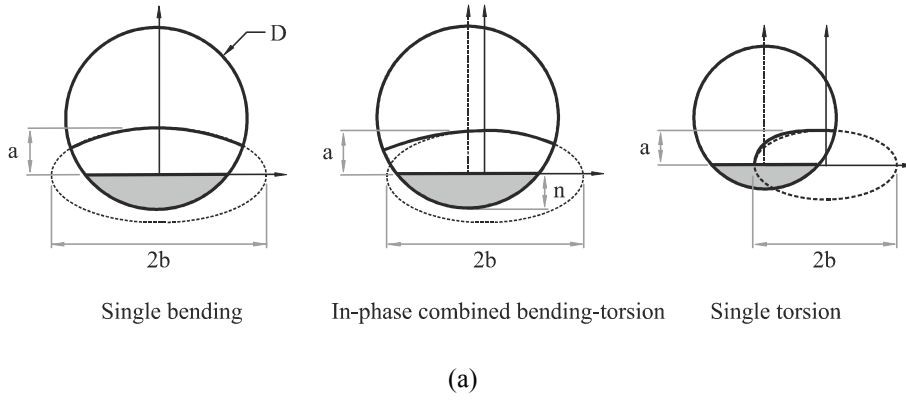
Figure 6. (a) Geometrical parameters; (b) crack aspect ratio (*a/b*) versus dimensionless crack length (*a/D'*)

The crack initiation length was defined using the El Haddad (1979) parameter expressed in the form

$$a_0 = \frac{1}{\pi} \left(\frac{\Delta K_{th}}{\Delta \sigma_0} \right)^2 \tag{1}$$

where ΔK_{th} is the range of the threshold value of the stress intensity factor and $\Delta \sigma_0$ is the fatigue limit stress range of the unnotched specimen. The two above-mentioned constants must be evaluated under the same stress ratio as the mechanical component to be assessed. Since the values of R are close to zero, but not exactly zero, such constants were determined on a case-by-case basis.

Regarding the ΔK_{th} value, the model of Klesnil and Lukas (1972) was applied to calculate it for each R value (see Eq. (2)). The ΔK_{th0} and x values were obtained from experimental data available in the literature (Luke, 2011). In relation to the $\Delta \sigma_0$ value, it was calculated for the different stress ratios from the fatigue limit at zero mean stress (R=-1) by applying the Goodman criterion. The fatigue limit at zero mean stress was evaluated using the Basquin equation (see Eq. (3)) obtained in a previous study (Branco, 2012) assuming a fatigue life (N_f) equal to 1×10^6 cycles. Thus, the values of a_0 found here were in the range of 121-129 μm.

$$\Delta K_{th} = \Delta K_{th0} (R - 1)^x \Leftrightarrow \Delta K_{th} = 7.12 \times (R - 1)^{0.87} \tag{2}$$

$$\sigma_a = \sigma_f' (2N_f)^b \Leftrightarrow \sigma_a = 1183.7 \times (2 \times 10^6)^{-0.0545} \Leftrightarrow \sigma_a = 536.8 \text{ MPa} \tag{3}$$

The number of cycles to crack initiation (N_i) for each case was calculated from the value of a_0 using experimental a-N curves. Since the crack growth was monitored at the notch surface, a relation between crack depth (a_0) and surface crack length ($2b_0$) was established. From the crack front shapes marked on the fracture surfaces, the typical crack aspect ratios (a_0/b_0) were about 0.8 (a_0 represents the deepest point of the crack front and $2b_0$ the surface crack length measured at the notch surface). Therefore, the corresponding values of $2b_0$ varied between 303-322 μm. In short, the number of cycles to crack initiation for each case was estimated using the experimental a-N curves obtained in the tests for surface crack lengths equal to $2b_0$.

The correlation between the number of cycles to crack initiation (N_i) and the local von Mises equivalent stress amplitude ($\Delta\sigma_{vML/2}$) was investigated. Figure 7 plots $\Delta\sigma_{vML/2}$ against N_i in a log-log scale. As can be seen, a very satisfactory linear correlation between those two variables was found. Note that the experimental results were fitted by linear regression with a relatively high correlation coefficient (r=0.938). These data were also used to obtain the design curve proposed by International Institute of Welding (i.e. 95% survival probability calculated from the mean value assuming two-sided confidence levels of 75%). The scatter band index (T_σ) for failure probabilities of 10% and 90% was equal to 1.406.

The fatigue life predictions were carried out from linear elastic finite element analyses. The notch effect on fatigue was accounted for using the Theory of Critical Distances (Taylor, 1999). The line method was used to average the elastic stress distribution over the critical region. In this method, the critical distance is defined as

$$D_{LM} = 2a_0 \tag{4}$$

where a_0 is the El Haddad parameter (see Eq. (1)) and D_{LM} is the critical distance for the line method. As referred to above, a specific value of a_0 was calculated to take into account the effective stress ratio of each test. In practice, D_{LM} varied between 242-258 μm.

The local von Mises equivalent stress was selected as representative of the fatigue failure process. As can be seen in Figure 7, it is able to correlate in a satisfactory way the resultant stress-strain states with the fatigue crack initiation lives. Figure 8(a) plots, as an example, the local von Mises equivalent stress (σ_{vML}) against the distance from the notch surface (d) for a specimen subjected to single bending. The results obtained show that the maximum stress occurs at the notch surface and then gradually decreases to an asymptotical value. The critical stress, calculated by applying the line method, corresponds to 928 MPa.

Figure 8(b) compares, in a dimensionless form, the stress profiles obtained for the different loading paths studied in this research. The local von Mises equivalent stress (σ_{vML}) was divided by its maximum value ($\sigma_{vML,max}$) and the distance from the notch surface (d) was divided by the critical distance (D_{LM}). Looking at the resultant stress-distance curves, it is possible to observe a first stage ($d/D_{LM} \leq 1$) with similar profiles and a second stage ($d/D_{LM} > 1$) in which the differences gradually increase with the dimensionless distance.
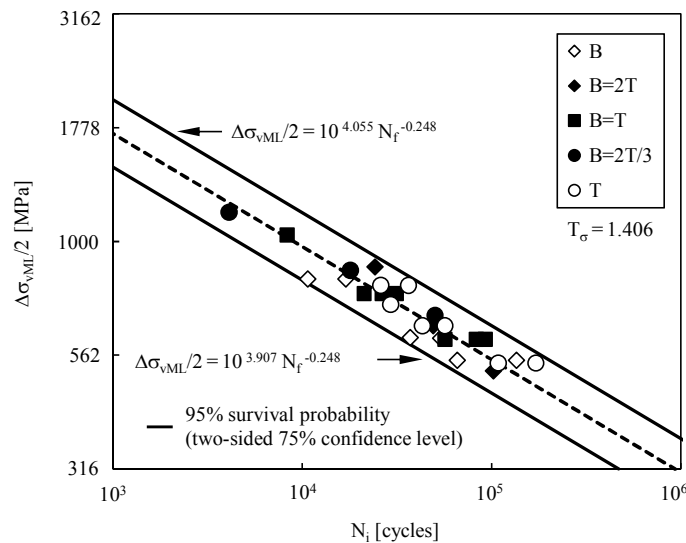

Figure 7. Local von Mises equivalent stress range versus number of cycles to crack initiation

The Coffin-Manson (CM) model was used to predict the fatigue crack initiation lives. In terms of local von Mises equivalent stress, this model can be formulated as follows

$$\frac{\Delta\varepsilon_{vML}}{2} = \frac{\sigma_f' - \sigma_{vML,m}}{E}(2N_f)^b + \varepsilon_f'(2N_f)^c \tag{5}$$

being $\Delta\varepsilon_{vML/2}$ is the averaged local von Mises equivalent strain amplitude, $\sigma_{vML,m}$ is the averaged mean local von Mises equivalent stress, E is the Young's modulus, σ_f' and b are the fatigue strength properties, and ε_f' and c are the fatigue ductility properties. All these properties are listed in Table 2.

The local stresses and strains for each test were calculated from the critical stress which was computed using the procedure described above. Figure 9(a) plots the experimental fatigue lives (N_i) obtained from the a-N curves for a crack length equal to a_0 against the predicted fatigue lives (N_p) obtained using the CM model. Two scatter bands for N_i/N_p ratios equal to 0.5 (i.e. $N_p = 2N_i$) and 2 (i.e. $N_i = 2N_p$) were also added in the figure. In general, fatigue
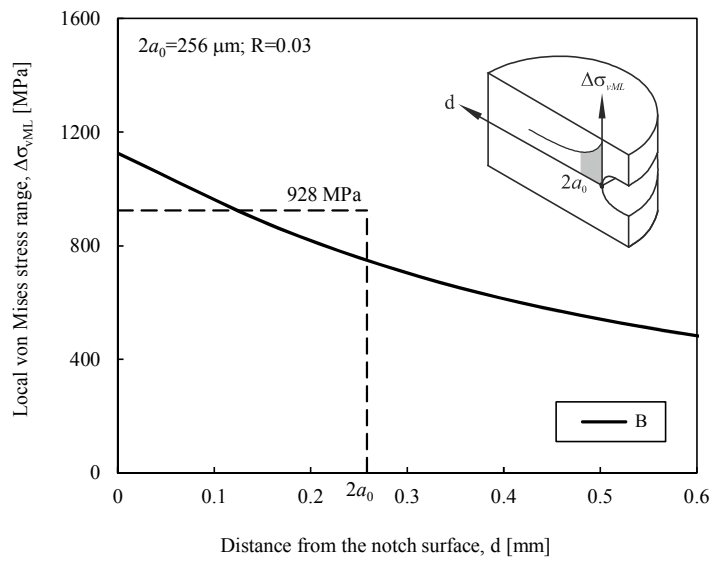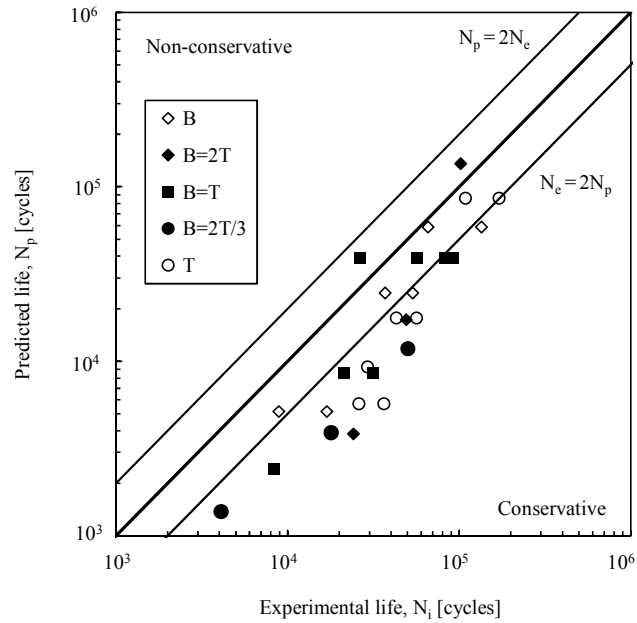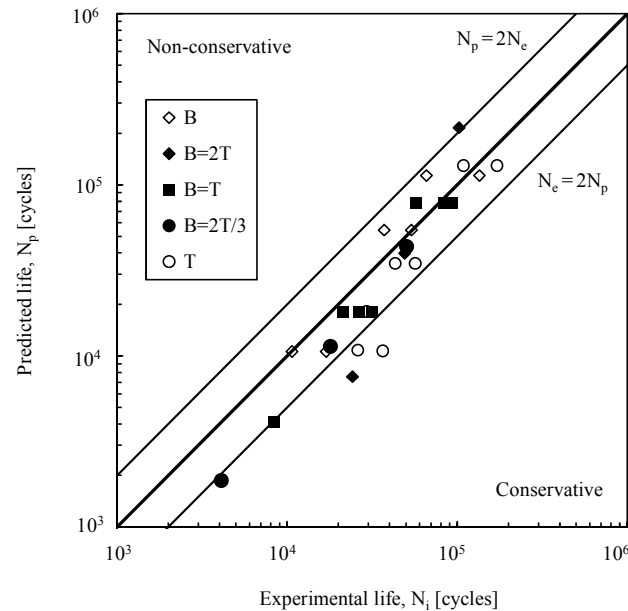

(a)
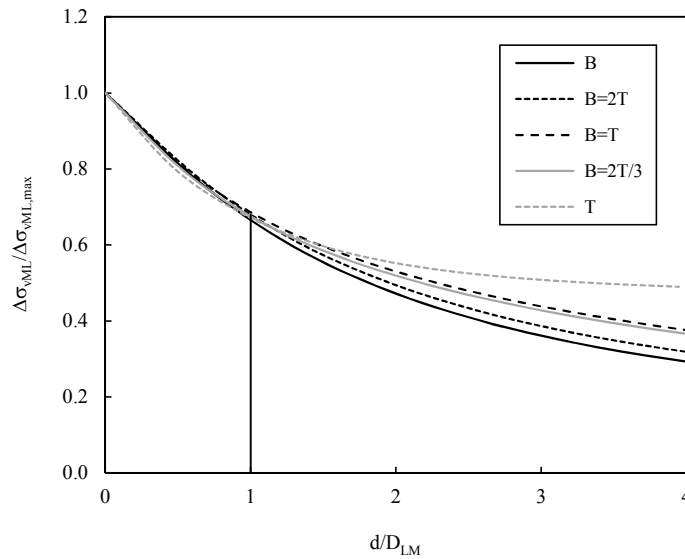
(b)

Figure 8. (a) $\Delta\sigma_{vmL}$ versus d for a specimen subjected to single bending; (b) dimensionless $\Delta\sigma_{vmL}$ versus dimensionless d for the different loading paths studied

(a)

(b)

Figure 9. Experimental versus predicted fatigue lives obtained by using the: (a) TCD; (b) ESED approaches.

life predictions in this range (i.e. $0.5 < N_p/N_i < 2$) are considered acceptable. As can be seen, the predictions calculated are close to the experimental values for predicted lives greater than about 2×10^4 cycles. In this region, a satisfactory linear correlation is obtained in a log-log scale. On the other hand, and not surprisingly, for shorter lives the predictions tend to be increasingly conservative. This fact is explained by an inadequate simulation of the local stress-strain field at the notch. In these cases, although the nominal stresses are elastic, the maximum stresses at the notch are inelastic.

In order to better simulate the local stress-strain field at the notch, the Equivalent Strain Energy Density (ESED) concept (Glinka, 1985) was applied. This concept assumes that the ratio of the strain energy density in the notch tip to the nominal strain energy density is the same in elastic or elastic-plastic straining. A typical stress-strain curve obtained using this approach for a single bending case is exhibited in Figure 10. Firstly, the stress and strain at the notch tip are calculated for the maximum loading (Point A). The maximum stress (σ_{max}) can be obtained using the following equation
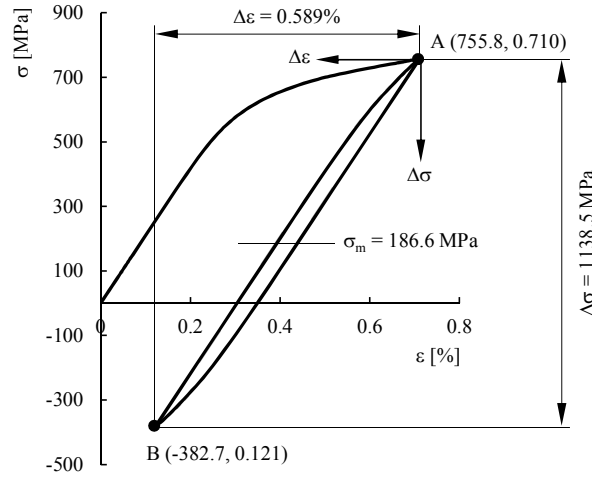
Figure 10. Hysteresis loops obtained for a single bending test by applying the ESED concept

$$\frac{\sigma_{max}^2}{2E} + \frac{\sigma_{max}}{n'+1}\left(\frac{\sigma_{max}}{k'}\right)^{1/n'} = K_T^2 \frac{\sigma_{n,max}^2}{2E} \tag{6}$$

where k' is the cyclic hardening coefficient, n' is the cyclic hardening exponent, K_T is the elastic stress concentration factor, $\sigma_{n,max}$ is the maximum nominal stress and E is the Young's modulus. In this research, the quantity $K_T \times \sigma_{max}$ was replaced by the maximum local von Mises stress ($\sigma_{vML,max}$) given by the FEM. This procedure avoided the calculation of the elastic stress concentration factors. The maximum strain (ε_{max}) was evaluated by substituting σ_{max} into the cyclic stress-strain curve given by

$$\varepsilon_{max} = \frac{\sigma_{max}}{E} + \left(\frac{\sigma_{max}}{k'}\right)^{1/n'} \tag{7}$$

being k' the cyclic hardening coefficient, n' the cyclic hardening exponent and E the Young's modulus. The stress and strain ranges were obtained with respect to an auxiliary coordinate system ($\Delta\sigma$, $\Delta\varepsilon$) with origin at point A (see Figure 5.55). The resultant stress range ($\Delta\sigma$) was found by solving the formula

$$\frac{\Delta\sigma^2}{4E} + \frac{\Delta\sigma}{n'+1}\left(\frac{\Delta\sigma}{2k'}\right)^{1/n'} = K_T^2 \frac{\Delta\sigma_n^2}{4E} \tag{8}$$

where k' is the cyclic hardening coefficient, n' is the cyclic hardening exponent, K_T is the elastic stress concentration factor, $\Delta\sigma_n$ is the nominal stress range and E is the Young's modulus. The strain range ($\Delta\varepsilon$) was determined from the basic cyclic stress-strain curve by applying a factor of 2, i.e.

$$\Delta\varepsilon = \frac{\Delta\sigma}{E} + 2\left(\frac{\Delta\sigma}{2k'}\right)^{1/n'} \tag{9}$$

being k' the cyclic hardening coefficient, n' the cyclic hardening exponent and E the Young's modulus.

The values of $\Delta\sigma$ and $\Delta\varepsilon$ for the case presented in Figure 10 account for the difference between both Point A and Point B in terms of stress and strain, respectively. The experimental fatigue lives (N_e) versus the predicted fatigue lives (N_p) for the loading paths studied here are presented in Figure 9(b). Two scatter bands for N_e/N_p ratios equal to 0.5 (i.e. $N_p=2N_e$) and 2 (i.e. $N_e=2N_p$) were also plotted. As can be seen, a large majority of data are inside the scatter bands, more specifically about 77% of the data. Besides, except for a single case of the B=2T series, the points outside the scatter bands are on the safe side (i.e. $N_i/N_p > 1$). It means that the amount of data inside the scatter bands or on the safe side is about 97%. Regarding the points outside the scatter bands, they tend to occur for predicted lives lower than 10^4 cycles in cases of single torsion and combined bending-torsion. On the other hand, for predicted lives greater than 10^4 cycles, the data are well correlated.

Tables 3 and 4 summarise, respectively, several statistical data obtained from the N_e/N_p values given by the TCD and ESED approaches, namely minimum N_e/N_p value, maximum N_e/N_p value, mean value, standard deviation and mean deviation. As can be seen, the N_e/N_p values for the TCD approach are within the range 0.68-6.38, with mean and standard deviation equal to 2.81 and 1.47, respectively. For the ESED approach, the N_e/N_p values vary between 0.47-3.41 and the mean and the standard deviation are, respectively, equal to 1.44 and 0.72. Furthermore, regardless of the model, the worst results in terms of standard deviation were found for B=2T. In opposition, the best standard deviations were obtained for single bending (B).

In order to better compare the values obtained by the two models, the fatigue prediction error (E_N) defined by following expression was determined

$$E_N = \log\left(\frac{N_e}{N_p}\right) \tag{10}$$

where N_e is the experimental life and N_p is the corresponding predicted life. The probability density functions of the fatigue prediction error obtained for the TCD and ESED approaches are presented in Figure 11. As can be

Table 3. Statistical data for the N_e/N_p values using the TCD approach

Tests	Minimum N_e/N_p	Maximum N_e/N_p	Mean	Standard deviation	Mean deviation
All tests	0.68	6.38	2.81	1.47	1.15
B	1.12	3.29	2.02	0.69	0.57
B=2T	0.76	6.34	3.31	2.30	2.01
B=T	0.68	3.67	2.32	0.97	0.77
B=2T/3	2.99	4.61	3.95	0.70	0.64
T	1.26	6.38	3.29	1.59	1.25

Table 4. Statistical data for the N_e/N_p values using the ESED approach

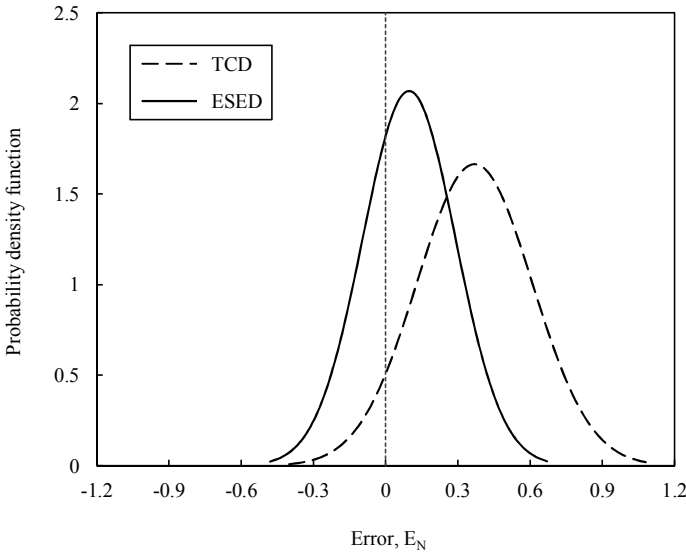| Tests	Minimum N_e/N_p	Maximum N_e/N_p	Mean	Standard deviation	Mean deviation
All tests	0.47	3.41	1.44	0.72	0.54
B	0.58	1.60	0.95	0.33	0.25
B=2T	0.47	3.20	1.64	1.15	1.04
B=T	0.73	2.02	1.34	0.40	0.34
B=2T/3	1.15	2.19	1.64	0.43	0.37
T	0.84	3.41	1.78	0.80	0.64

Figure 11. Probability density functions of fatigue life predictions for the TCD and ESED approches

seen, the latter gives much better results than the former. In both cases, the errors tend to be moved to the safe side. Nevertheless, the results obtained with the ESED model are closer to a mean error equal to zero than the TCD model.

5   Conclusions

A comparative study of fatigue life predictions obtained from both the Theory of Critical Distances (TCD) and Equivalent Strain Energy Density (ESED) approaches was carried out in lateral notched round bars subjected to in-phase combined bending-torsion loading. The following conclusions can be summarised as follows:

- A significant influence of the loading path on the surface crack trajectories and initiation sites was found. In the absence of shear stress, the crack grows in a direction normal to the axis of the specimen and the crack initiates at the centre of the notch. When the shear stress to the normal stress ratio increases, the surface crack trajectories tend to be more curved and the crack initiates closer to the curved edge of the notch.
- The local von Mises equivalent stress seems to be adequate to correlate the resultant stress-strain states at the notch with the fatigue crack initiation life. Regardless of the loading pattern, a very satisfactory linear correlation was found in a log-log scale between the local von Mises equivalent stress range and fatigue crack initiation life.
- The fatigue life predictions obtained with the TCD approach were too conservative for lower lives, i.e. lower than 10^4 cycles and were in line with the experimental results for higher lives. With regard to the ESED approach, the predictions and the experimental values were well correlated in all the range studied in this research. However, for lower lives, the predictions tend to be slightly conservative.

References

Abreu, L. M. P.; Costa, J. D.; Ferreira J. M.: Fatigue behaviour of AlMgSi tubular specimens subjected to bending-torsion loading. *International Journal of Fatigue*, 31, (2009), 1327-1336.

Branco, R.; Costa, J. D.; Antunes, F. V.: Low-cycle fatigue behaviour of 34CrNiMo6 high strength steel. *Theoretical and Applied Fracture Mechanics*, 58, (2012), 28-34.

Costa, J. D.; Abreu, L. M. P.; Pinho, A. C. M.; Ferreira, J. M.: Fatigue behaviour of tubular AlMgSi welded specimens subjected to bending-torsion loading. *Fatigue and Fracture of Engineering Materials and Structures*, 28, (2005), 399-407.

El Haddad, M. H.; Topper, T. H.; Smith, K. N.: Prediction of non propagating cracks. *Engineering Fracture Mechanics*, 11, (1979), 573-584.

Eliaz, N.; Sheinkopf, H.; Shemesh, G.; Artzi, H.: Cracking in cargo aircraft main landing gear truck beams due to abusive grinding following chromium plating. *Engineering Failure Analysis*, 12, (2005), 337-347.

Espadafor, F.; Villanueva, J.; García, M.: Analysis of a diesel generator crankshaft failure. *Engineering Failure Analysis*, 16, (2009), 2333-2341.

Fash, J. W.; Socie, D. F.; McDowell, D. L.: Fatigue life estimates for a simple notched componente under biaxial loading. Multiaxial Fatigue, STP 853, Edited by Miller, K. and Brown, M., *American Society for Testing and Materials*, (1985), 497-513.

Firat, M.: A numerical analysis of combined bending-torsion fatigue of SAE notched shaft. *Finite Elements in Analysis and Design*, 54, (2012), 16-27.

Garud, Y.S.: Multiaxial fatigue: a survey of the state-of-art. *Journal of Testing and Evaluation*, 9, (1981), 165-178.

Glinka, G.: Calculation of inelastic notch-tip strain-stress histories under cyclic loadings. *Engineering Fracture Mechanics*, 22, (1985), 839–854.

Gough, H. J.: Engineering steels under combined cyclic and static stresses. *Institution of Mechanical Engineers*, 160, (1949), 417-440.

Griza, S.; Bertoni, F.; Zanon, G.; Reguly, A.; Strohaecker, T.: Fatigue in engine connecting rod bolt due to forming laps. *Engineering Failure Analysis*, 16, (2009), 1542-1548.

Klesnil, M.; Lukas, P.: Effect of stress cycle asymmetry on fatigue crack growth. *Materials Science and Engineering*, 9, (1972), 231-240.

Luke, M.; Varfolomeev, I.; Lütkepohl, K.; Esderts, A.: Fatigue crack growth in railway axles: Assessment concept and validation tests. *Engineering Fracture Mechanics*, 78, (2011), 714-730.

Park, J.; Nelson, D. V.: In-phase and out-of-phase combined bending-torsion fatigue of a notched specimen. Multiaxial Fatigue and Deformation: Testing and Prediction. ASTM STP 1387, Edited by Kalluri, S. and Bonacuse, P. J., *American Society for Testing and Materials*, (2000), 246-265.

Savković, M.; Gašić, M.; Petrović, D.; Zdravković, N.; Pljakić, R.: Analysis of the drive shaft fracture of the bucket wheel excavator. *Engineering Failure Analysis*, 20, (2012), 105-117.

Socie, D., Marquis, G.: Multiaxial Fatigue. *Society of Automotive Engineers*, (2000), ISBN: 0-7680-0453-5.

Tartaglia, J.; Hayrynen, K.: A Comparison of fatigue properties of austempered versus quenched and tempered 4340 steel. *Journal of Materials Engineering and Performance*, 21, (2012), 1008-1024.

Taylor, D.: Geometrical effects in fatigue: a unifying theoretical model. *International Journal of Fatigue*, 21, (1999), 413-420.

Tipton, S. M.; Nelson, D. V.: Fatigue life predictions for a notched shaft in combined bending and torsion. Multiaxial Fatigue, STP 853, Edited by Miller, K. and Brown, M., *American Society for Testing and Materials*, (1985), 514-550.

Witek, L.: Failure analysis of the wing-fuselage connector of an agricultural aircraft. *Engineering Failure Analysis*, 13, (2006), 572-581.

You, B. R.; Lee, S. B.: A critical review on multiaxial fatigue assessment of metals. *International Journal of Fatigue*, 18, (1996), 235-244.

Yu, Z.; Xu, X.: Failure analysis of connecting bolts and location pins assembled on the plate of main-shaft used in a locomotive turbochanger. *Engineering Failure Analysis*, 15, (2008), 471-479.

Yu, Z.; Xu, X.: Failure analysis of a locomotive turbocharger main-shaft. *Engineering Failure Analysis*, 16, (2009), 495-502.

Address:

R. Branco, Polytechnic Institute of Coimbra, ISEC, Department of Mechanical Engineering, 3030-199 Coimbra, Portugal, email: rbranco@isec.pt